

Wideband Quasi-Nondiffraction Beam With Accurately Controllable Propagating Angle and Depth-of-Field

Yi Chen Zhong and Yu Jian Cheng, *Senior Member, IEEE*

Abstract—A wideband phase shift surface (PSS) antenna is proposed in this paper, which launches quasi-nondiffraction beam with accurately controllable inclination angle and depth-of-field. First, a novel method to generate the off-axis quasi-nondiffraction beam in an arbitrary direction is proposed. It modifies and further combines the design methods of the off-axis focusing antenna and the zero-order Bessel beam antenna. This method is helpful to improve the design precision of the depth-of-field of the beam. Then, one kind of hexagonal patch is employed as the element of the PSS. Its phase shift compensation capability can increase the bandwidth and improve the stability of the performance of the antenna over a wideband from 27 to 31 GHz. The results of numerical simulation, full-wave simulation, and experiment show that the proposed antenna can effectively generate the expected beam.

Index Terms—Large depth-of-field, nondiffraction beam, off-axis focusing, phase shift surface (PSS) antenna, wideband.

I. INTRODUCTION

QUASI-NONDIFFRACTION beam has been employed in applications such as near-field high-speed communication, imaging, directional heating, and wireless energy transmission [1]. The quasi-nondiffraction beam has the advantages of free focus, energy directional transmission, and controllable range of action [2]. However, propagating direction of the previous quasi-nondiffractive beam is usually broadside direction. It is then desirable to obtain an off-axis propagating quasi-nondiffraction beam with controllable propagating direction and depth-of-field (i.e., nondiffraction range) in the near-field region. Meanwhile, a broader bandwidth with stable beam direction and depth-of-field is also expected.

The quasi-nondiffractive beam has many forms. Among them, the most commonly used is the zero-order pesudo-Bessel beam [3], which is an ideal method to realize the

Manuscript received May 4, 2017; accepted July 26, 2017. Date of publication August 7, 2017; date of current version October 5, 2017. This work was supported in part by the National Natural Science Foundation of China under Grant 61622105, in part by the Science Foundation for Distinguished Young Scholars of Sichuan Province under Grant 2015JQ0005, in part by Fundamental Research Funds for the Central Universities under Grant ZYGX2014Z008, in part by the National Natural Science Foundation of China under Grant 61631012, and in part by the National Program for Support of Top-Notch Young Professionals (*Corresponding author: Yu Jian Cheng*.)

The authors are with the EHF Key Laboratory of Fundamental Science, School of Electronic Engineering, University of Electronic Science and Technology of China, Chengdu 611731, China (e-mail: chengyujian@uestc.edu.cn).

Color versions of one or more of the figures in this paper are available online at <http://ieeexplore.ieee.org>.

Digital Object Identifier 10.1109/TAP.2017.2736536

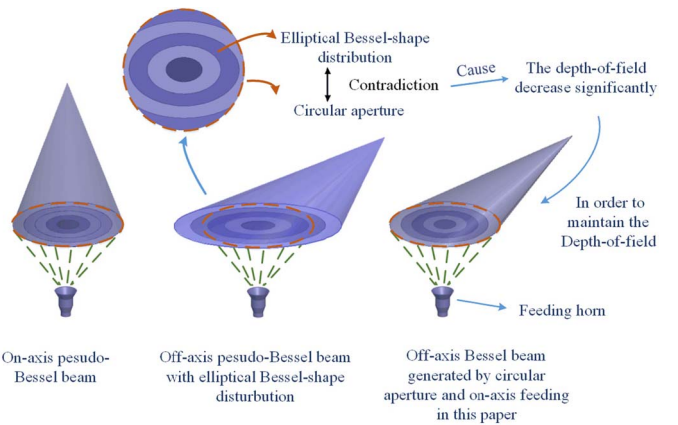


Fig. 1. Schematic of the off-axis nondiffraction beam generated on a circular aperture.

beam with a large depth-of-field. Several techniques to launch the zero-order pseudo-Bessel beam were proposed in [3]–[17]. It is worth noting that all of these pesudo-Bessel beams are perpendicular to the aperture.

The common method to generate a tilted Bessel beam is to project the Bessel distribution onto a tilted plane so as to obtain the desired aperture field distribution, and then realize the field distribution on the aperture of antenna [18]. However, the projection of the axisymmetric Bessel beam on an inclined surface is elliptical. Not only does the elliptical aperture antenna face the problem of asymmetric feeding, but the shape of the elliptical aperture (i.e., axis ratio) also needs to be changed in regard to the preset inclination angle of the beam.

To solve the problems, a simple method is to cut out a circular aperture on the required elliptical aperture field distribution, as shown in Fig. 1. However, due to the incomplete Bessel distribution on the outer rings which are cut by the circle, the depth-of-field of the beam will seriously decrease since the nondiffraction characteristic of the beam is destroyed at the end of the beam.

In this paper, a novel method, which can generate the quasi-nondiffraction beam with arbitrary propagation direction and depth-of-field on a circular aperture, is proposed. It can maintain nondiffraction characteristics at the end of the beam to achieve a good nondiffraction beam with the accurate depth-of-field. The design methods of the zero-order pesudo-Bessel beam antenna and the off-axis multifocusing antenna

are combined and modified. The aperture of the antenna is divided into a number of concentric rings. The field in each ring is focused on one single point along an off-axis line. The relative phase difference between rings satisfies the phase distribution of the zero-order pesudo-Bessel beam.

The phase-shifting surface (PSS) [4], [5], [19] is employed to transform the quasi-Gauss beam, launched by a linear polarized feeding horn, to the same polarized off-axis quasi-nondiffraction beam, which is achieved by changing the phase of the transmitted field. The PSS only controls the phase shift between the incident and transmitted wave while keeping the amplitude almost unchanged.

For a near-field focusing antenna, the bandwidth should be considered as well. As is well known, the phase shift of each element on the PSS changes with the frequency. To achieve a wide bandwidth, the PSS element should have the phase shift compensating ability in the entire band. A new kind of three-layer hexagonal patch is proposed to satisfy the required phase distribution within a wide band. The least mean square error algorithm is used to synthesize the PSS element in order to obtain the minimum phase shift error in the entire band. Besides, since the selected PSS elements are insensitive to the polarized direction of the incident field, the polarization of the beam is determined by that of the feeding horn. In this way, it would be easy to realize the linear, circular, or elliptical polarized beams. The results of numerical simulation, full-wave simulation, and experiment agree well with each other. The synthesized antenna can effectively generate the beam with predictable and controllable depth-of-field and inclination angle in the entire band.

II. FUNDAMENTS OF THE OFF-AXIS QUASI-NONDIFFRACTION BEAM ANTENNA

The operation principle of the proposed antenna is shown in Fig. 1. The PSS is illuminated by a quasi-Gauss beam which is emitted from the feeding horn and has the quasi-spherical wavefront. A three-layer wideband PSS, which is polarization-insensitive, is used to transform the quasi-spherical wave to the off-axis quasi-nondiffraction beam.

The required phase shift of the PSS is derived as follows. As shown in Fig. 1, the PSS is divided into a number of concentric rings. By designing the phase distribution of the transmitted field from PSS, the transmitted field in each ring is focused on a single point in the off-axis line. With the increase of the radius, the focus points are distributed evenly along the target line. The most outer ring focuses on the ending point of the preset depth of field, and the most inner ring is on the starting point. Thus, the relative phase differences of the points in one ring can be obtained.

Another important issue is the relative phase differences between these rings. If the relative phase differences between the rings are not specified, the depth-of-field of the beam will have considerable gap from the expected value. So to determine the relative phase differences between the rings, the principle of the zero-order pesudo-Bessel beam is employed and modified.

The pesudo-Bessel beam can be generated by a group of inward cylindrical traveling waves with wave vectors lying

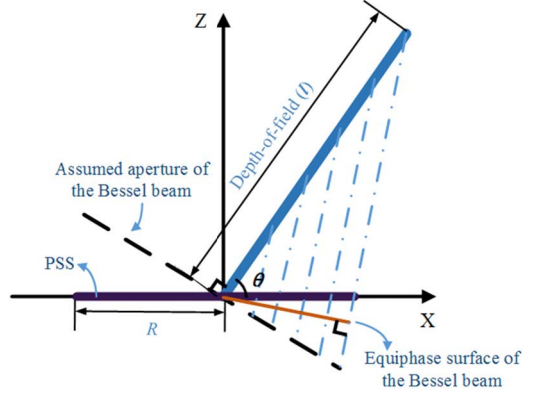


Fig. 2. Sketch map of calculating the pesudo-Bessel-beam-like phase distribution on the positive half of the x -axis.

on a cone [3]. As described above, the aperture field distribution of an off-axis Bessel beam is elliptical. It cannot be completely generated by a circular aperture. Thus, the non-diffraction characteristics of the beam are destroyed at the end of the beam, and consequently, the depth-of-field of the beam is decreased. In order to overcome this problem, the design methods of the off-axis multifocusing antenna and the zero-order pesudo-Bessel beam antenna are combined and modified. The phase distribution on the radial line along the inclined direction of the beam on the aperture is set to satisfy the phase distribution of the zero-order pesudo-Bessel beam. Thus, the relative phase between rings can be determined.

From the above theory, the phase distribution on the PSS can be derived. The beam is assumed to be tilted toward the positive half of the x -axis. As shown in Fig. 2, the aperture of the Bessel beam is assumed to be perpendicular to the beam. The theory of the zero-order pseudo-Bessel beam claims that the equiphase surface of the pseudo-Bessel beam is perpendicular to the wavefront of the converging beams. Based on this equiphase surface and the phase of the quasi-spherical wave from the feeding horn, the phase shift of the PSS on the positive half of the x -axis can be derived as

$$\varphi_1(f) = 2\pi \frac{f}{c} \left[\frac{\sqrt{d^2 + r^2} - d}{\sqrt{l^2 + R^2 - 2lR \cos \theta}} + \frac{(-r) \times (l \cos \theta - R)}{\sqrt{l^2 + R^2 - 2lR \cos \theta}} \right]. \quad (1)$$

In (1), $\varphi_1(f)$ is the ideal phase shift of the PSS element which is located at the positive half of the x -axis and has a radius of r from the center of the PSS at a frequency of f . c is the velocity of wave in free space, d is the distance from the phase center of feeding horn to the PSS, R is the radius of the PSS, l is the target depth-of-field of the beam, and θ is the target angle between the off-axis beam and the PSS.

The phase shift calculated above determines the relative phase shift differences between the rings first. The next step is to obtain the relative phase shifts of the points in one ring. As mentioned above, the field in each ring is focused on one single point. Then the relative phase shifts of the points in one ring can be derived as follows.

The x -value of the target point focused by the field radiating from the ring with a radius of r on the aperture is

$$r_s = \frac{l \cos \theta}{R} r. \quad (2)$$

The relative phase shift of each point in the ring with a radius of r is

$$\varphi_2(f) = 2\pi \frac{f}{c} \left[\sqrt{(x - r_s)^2 + y^2 + \left(\frac{lr \sin \theta}{R} \right)^2} - \sqrt{(r - r_s)^2 + \left(\frac{lr \sin \theta}{R} \right)^2} \right]. \quad (3)$$

In (2) and (3), x and y are the x -value and y -value of the points on the PSS, respectively, $r = \sqrt{x^2 + y^2}$. φ_2 is normalized as 0° on the positive half of the x -axis. $\sqrt{(x - r_s)^2 + y^2 + (r_s \tan \theta)^2}$ is the distance between the point on the aperture and its focusing point on the target line. $\sqrt{(r - r_s)^2 + (r \tan \theta)^2}$ is the distance between the point on the x -axis and its focusing point. Finally, the target phase shift on the PSS is

$$\varphi(f) = \text{mod}[(\varphi_1 + \varphi_2), 2\pi]. \quad (4)$$

φ is the phase of the incident wave minus the phase of the transmitted wave on the PSS, which is normalized to the range of $[0, 2\pi]$. For an antenna with a predetermined aperture, the inclination angle θ and the depth-of-field l are the two main parameters in the design. They can control the inclination angle and the depth-of-field of the beam independently. The depth-of-field is defined as the length of the beam, which is within the 3 dB attenuation of the maximum magnitude of electric fields in the beam.

Next, the numerical simulation implemented by MATLAB is employed to verify the beam, which is generated by the phase distribution as calculated in (4). The polarization direction of the wave from the feeding horn is assumed to be along the y -axis, and all the electric field mentioned in this paper refers to the y -polarized field. In simulation, the PSS is assumed to be a circular surface with a diameter of 200 mm, which is located at -100 – 100 mm on the x -axis and y -axis. The incident wave is assumed as a Gaussian beam with -10 dB illumination level at the edge of the PSS. The operating frequency is 29 GHz. The z -coordinate ranges from 5 to 300 mm.

As shown in Fig. 3, θ can control the direction of the generated beam accurately in the near-field region. Meanwhile, with the increase of θ , the beam can always be kept in a straight line and its depth-of-field almost keeps unchanged. In other words, the inclination angle and the depth-of-field can be controlled independently. In Fig. 3(a), when the beam is pointing at the axial direction, the generated beam is a zero-order pseudo-Bessel beam. Its field distribution on the aperture is the same as that of an axicon lens which works as a pseudo-Bessel beam launcher. The symmetry of the Bessel-shape distribution is gradually affected with the decrease of the inclination angle. With the increase of the inclination angle, the beam moves closer to the radiating aperture. The asymmetric interference in the region close to the aperture is relatively stronger.

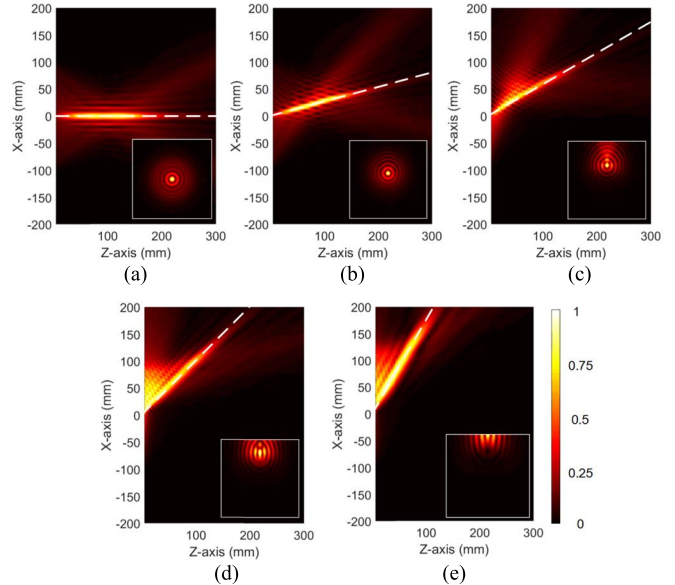


Fig. 3. Normalized magnitudes of the electric fields in the XOZ -plane when the Gaussian beam is incident upon the PSS. The phase shift of the PSS is calculated by (1)–(4) with $l = 200$ mm and various θ . (a) $\theta = 90^\circ$. (b) $\theta = 75^\circ$. (c) $\theta = 60^\circ$. (d) $\theta = 45^\circ$. (e) $\theta = 30^\circ$. The white dashed lines are the preset beam directions with different θ . Small squares in figures are the magnitude of the electric field in xy plane with $x = -100$ – 100 mm, $y = -100$ – 100 mm, and $z = 60$ mm.

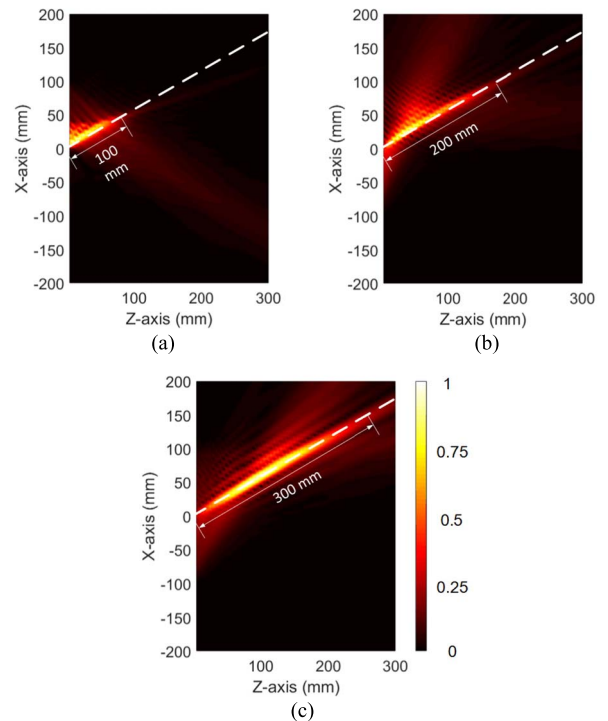


Fig. 4. Normalized magnitudes of the electric field in the XOZ -plane when a Gaussian beam is incident upon the PSS. The phase shift of the PSS is obtained by (1)–(4) with $\theta = 60^\circ$ and various depth-of-field l . (a) $l = 100$ mm. (b) $l = 200$ mm. (c) $l = 300$ mm.

The depth-of-field of the beam can only be controlled by l in (1)–(3). As shown in Fig. 4, the inclination angle of the beam is preset as 60° . The PSS is designed by (1)–(4) with

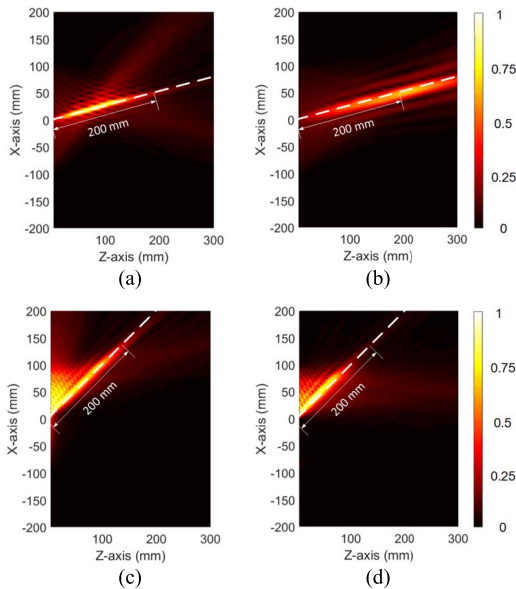


Fig. 5. Normalized magnitudes of the electric field in the $X Oz$ -plane with $l = 200$ mm. (a) $\theta = 75^\circ$. (b) $\theta = 75^\circ$. (c) $\theta = 45^\circ$. (d) $\theta = 45^\circ$. (a) and (c) are the fields of the multifocusing antennas with the Bessel-beam-like phase distribution on the positive half of the x -axis. (b) and (d) are the fields of the multifocusing antennas without the Bessel-beam-like phase distribution.

different l . The transmitted field from the PSS shows that l can control the depth-of-field accurately while keeping the inclination angle of the beam unchanged.

The field evenly focusing along the target line within the depth-of-field, as shown in (2) and (3), is easy to be understood. However, the Bessel-beam-like phase distribution on positive half of the x -axis, which is calculated by (1), has to be evaluated.

Fig. 5 shows the difference between the profiles of the multifocusing antenna with and without the Bessel-beam-like phase distribution on the aperture. The antenna without the Bessel-beam-like phase distribution means that the phase of the field along the positive half of x -axis on the aperture maintains 0° . In this case, the aperture field distribution is given by (2)–(5)

$$\varphi_1(f) = 2\pi \frac{f}{c} (\sqrt{d^2 + r^2} - d). \quad (5)$$

This kind of phase distribution is a focusing system which focuses along an off-axis line within the depth-of-field. However, the depth-of-field of the generated beam is inconsistent with the design value. As shown in Fig. 5, on one hand, when $\theta = 45^\circ$, the generated depth-of-field from the pure multifocusing antenna is significantly smaller than the target value; on the other hand, it is much larger than the target value if $\theta = 75^\circ$. In this case, the depth-of-field and the direction of the beam cannot be controlled independently. In addition, the generated beam is wider and the focusing effect is worse. This illustrates the advantage of employing the phase distribution of the pseudo-Bessel beam in the design.

Next, the electric field distributions of the modified off-axis nondiffraction beam in this paper are compared with those of the traditional off-axis Bessel beam. These two beams

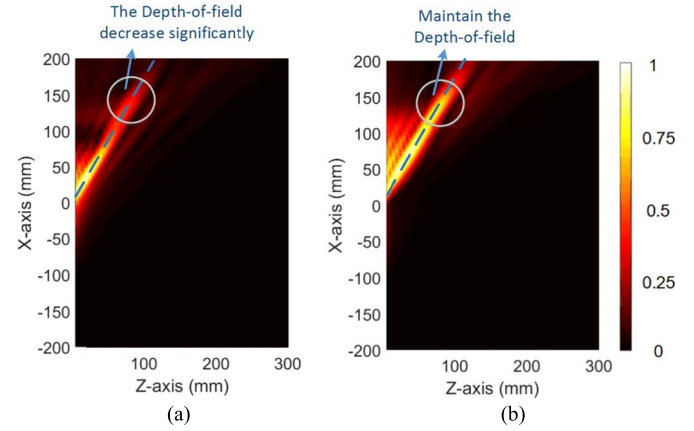


Fig. 6. Normalized magnitudes of the electric fields in the $X Oz$ -plane at 29 GHz with $l = 200$ mm, $\theta = 30^\circ$, and $D = 200$ mm. D is the diameter of PSS. (a) Traditional off-axis Bessel beam. (b) Modified nondiffraction beam in this paper.

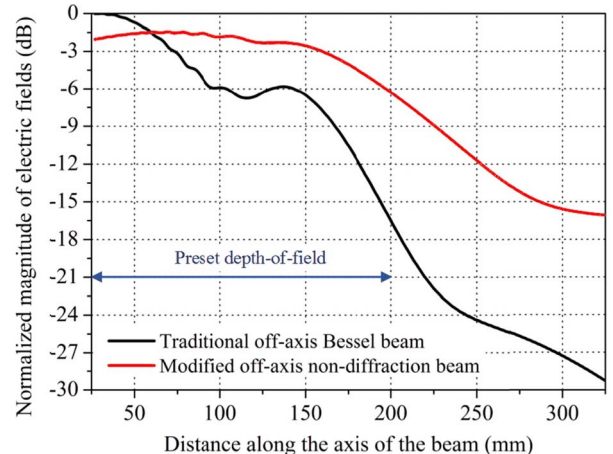


Fig. 7. Normalized magnitudes of the electric fields along the axis of the beam (i.e., along the dashed blue line in Fig. 6) at 29 GHz with $l = 200$ mm, $\theta = 30^\circ$, and $D = 200$ mm.

differ in the aperture phase distributions and the difference will become more and more obvious with the decrease of the inclination angle θ . Thus the inclination angle θ is set as small as 30° in the comparison. As shown in Figs. 6 and 7, compared with the traditional off-axis Bessel beam distribution (i.e., realize a Bessel beam distribution on a tilted circular plane), the modified nondiffraction beam in this paper can maintain desirable nondiffraction characteristics at the end of the beam so that a good nondiffraction beam with considerable depth-of-field can be achieved.

III. DESIGN PROCEDURE

In the application of imaging or high-speed communication, a millimeter-wave and wideband antenna is often expected [20]–[23]. However, in the near-field focusing systems, the focused points may deviate from the preset position when the operating frequency deviates from the center frequency. Therefore, the effect of the frequency deviation on the performance of the proposed antenna should be evaluated. As an off-axis nondiffraction beam antenna, the bandwidth of

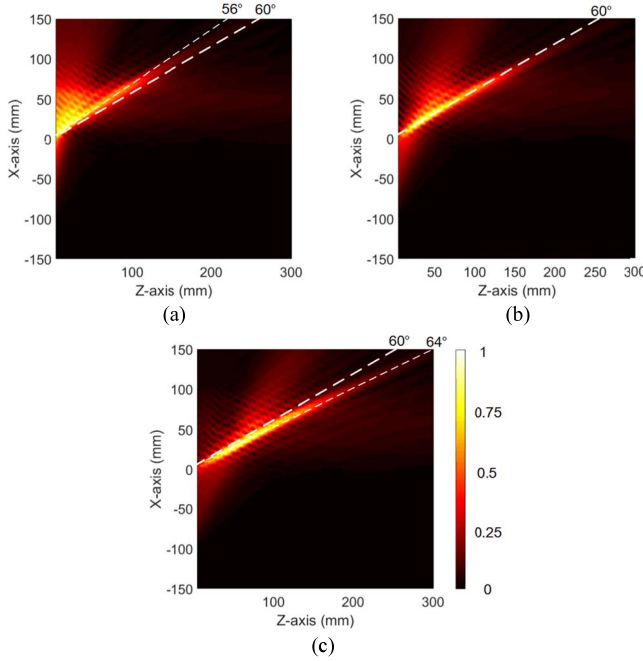


Fig. 8. Normalized magnitudes of the electric fields in the XOZ -plane when the PSS antenna is operating at different frequencies. (a) $f = 27$ GHz. (b) $f = 29$ GHz. (c) $f = 31$ GHz. The phase shift of the PSS is obtained by (1)–(4) with $\theta = 60^\circ$, $l = 200$ mm, $d = 173$ mm, and $f = 29$ GHz.

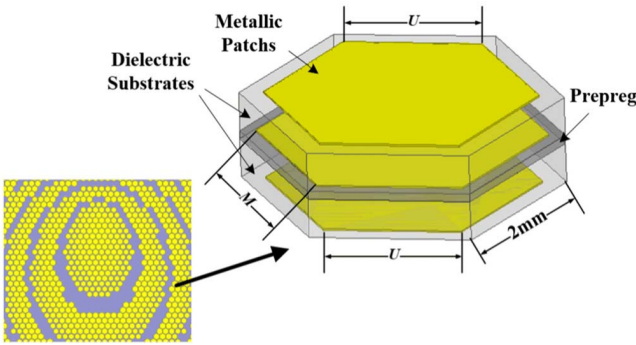


Fig. 9. Hexagonal PSS element.

the antenna is determined in a way that the variation range of the inclination angle of the beam is less than 3° . As shown in Fig. 8, if there is no special design on the phase-frequency response of the PSS, the variation range of the inclination angle will be up to 8° in the band of 27–31 GHz. Besides, the depth-of-field and the radiation efficiency of the antenna should be taken into consideration as well. The variation range of the depth-of-field should be less than 10% of the maximum value in the band, and the radiation efficiency should be higher than 50% within the bandwidth. In Fig. 8, the phase shift of the PSS elements is calculated at 29 GHz, which is assumed to stay unchanged over the whole band. As can be seen, the frequency offset results in a variation in the inclination angle within the range of 56° – 64° . Thus, in order to keep the inclination angle of the beam unchanged, the PSS element needs to have the phase shift compensating ability in the band.

A three-layer hexagonal patch [4], as shown in Fig. 9, is employed as the PSS element in this work. Its operation

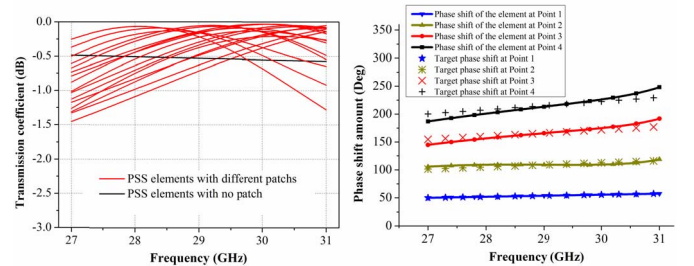


Fig. 10. (a) Full-wave simulated magnitudes of the transmission coefficients of all the elements employed after the optimization. (b) Normalized full-wave simulated phase shifts of the PSS elements placed at Point 1 ($x = 0$ mm, $y = 6$ mm), Point 2 ($x = 0$ mm, $y = 6$ mm), Point 3 ($x = 0$ mm, $y = 9$ mm), and Point 4 ($x = 0$, $y = 11.5$ mm). The parameters of the elements at these positions are Point 1 ($U = 1.65$ mm, $M = 1.6$ mm), Point 2 ($U = 1.5$ mm, $M = 1.45$ mm), Point 3 ($U = 1.25$ mm, $M = 1.05$ mm), and Point 4 ($U = 0$ mm, $M = 0$ mm).

frequency band is from 27 to 31 GHz. It consists of three layers of metal and two layers of substrate. Two Taconic TLY-5 dielectric substrates ($\epsilon_r = 2.20$, $\tan \delta = 0.0009$, $h = 0.508$ mm) are used and bonded by a prepreg sheet (Taconic FR-28, $\epsilon_r = 2.75$, $\tan \delta = 0.0009$, $h = 0.109$ mm). The phase shift of the element is determined by the size of the hexagonal patches. U and M are side lengths of the hexagonal patches. The phase shift of this element changes with the frequency, and its phase-frequency response curve can be adjusted in a certain range. Therefore, this kind of element has the phase shift compensating ability in the band. In addition, since the element is insensitive to the polarization of the incident wave, the polarization of the outgoing wave will only depend on the feeding horn. Thus, the PSS has the ability to realize the beam with different polarizations.

The elements are optimized by the least mean square error algorithm mentioned in [5], in order to minimize the phase shift error over the entire band. The principle is to make the phase shift error between the actual phase shift and the target one as small as possible in the entire band while the high transmission efficiency is kept in the band. The lower boundary of transmission coefficients in optimizations is set as -2 dB. The elements, of which the transmission loss is higher than 2 dB in the band, will be abandoned. The transmission coefficients of all the elements used in the final design are shown in Fig. 10(a). They range from -1.46 dB to -0.031 dB. Thus, the most suitable element can be placed at each position on the PSS. In other words, using this method enables the elements to get a certain ability to compensate the target phase shift in the entire band [5]. Fig. 10(b) shows the phase shift values of these elements at different positions of the PSS. The elements are simulated by Ansys HFSS with the Floquet model. The phase shift values of these elements increase with the frequency and keep track with the target phase shifts calculated by (1)–(4). Although there is still a deviation between the actual phase shift and the target value, the deviation has been reduced to the minimum value by using the optimization algorithm. This will help the antenna to achieve a stable performance over a wideband.

The magnitudes and phases of the transmission coefficients of four different elements with different incident angles are

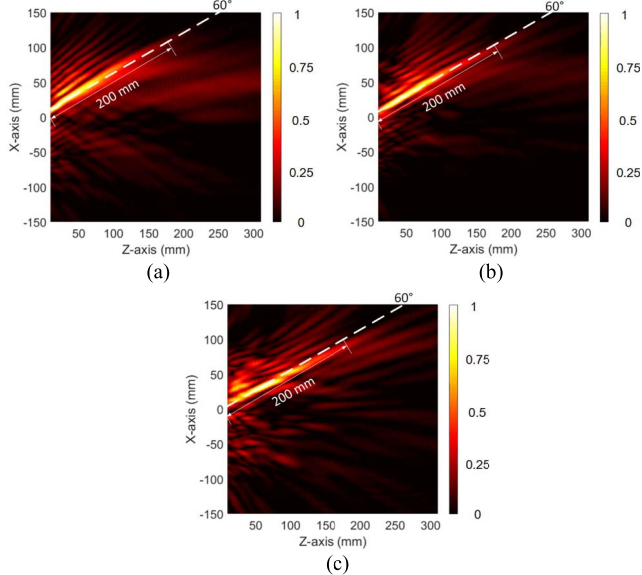


Fig. 11. Full-wave simulated normalized magnitudes of the electric fields in the $X Oz$ -plane at different frequencies. (a) $f = 27$ GHz. (b) $f = 29$ GHz. (c) $f = 31$ GHz. The distribution of the PSS elements is obtained by (1)–(4) with $\theta = 60^\circ$ and $l = 200$ mm.

obtained by full-wave simulations. At different incident angles, the magnitudes of the transmission coefficients of all elements change less than 0.35 dB and the phases change less than 22° . Thus, the performance of the PSS element is almost unchanged when the incident angle is less than 30° .

Next, the whole antenna is modeled and full-wave simulated by Ansys HFSS. The diameter of the PSS is 200 mm, and $d = 173$ mm. Full-wave simulated magnitudes of the electric fields in the $X Oz$ -plane at different frequencies are shown in Fig. 11. As mentioned above, the frequency offset results in variations in the inclination angle and the depth-of-field. The phase compensation capability of the element helps to reduce these variations. The simulated beam directions agree well with the preset values, and the deviations are within 2° . These deviations are mainly caused by the incomplete phase shift compensation. The phase-shifting compensation fails at positions without the phase shift element (e.g., Point 4 in Fig. 10). Thus, the phase shift has not been compensated at those positions.

The full-wave simulation results of the antennas with different l and θ at the center frequency are shown in Figs. 11(b) and 12. The propagating angle and the depth-of-field are accurately controlled. They are in agreement with the numerical simulations shown in Figs. 3 and 4. The maximum differences of them are 0.268, 0.325, and 0.312, respectively. Their main beams are completely coincident, but the sidelobes in the full-wave simulation are relatively higher due to the mutual coupling between the elements and the surface wave on the PSS.

IV. EXPERIMENTAL RESULTS

A prototype antenna is fabricated as shown in Fig. 13. The vector network analyzer (VNA) Agilent N5244N is employed in the experiment [24], [25]. One port of the VNA is connected

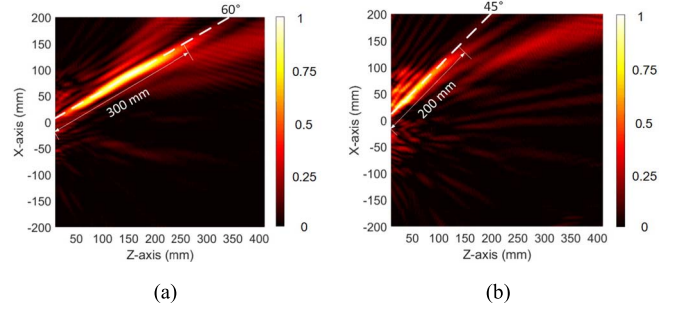


Fig. 12. Full-wave simulated normalized magnitudes of the electric fields in the $X Oz$ -plane at the frequency of 29 GHz. (a) $\theta = 60^\circ$ and $l = 300$ mm. (b) $\theta = 45^\circ$, and $l = 200$ mm.

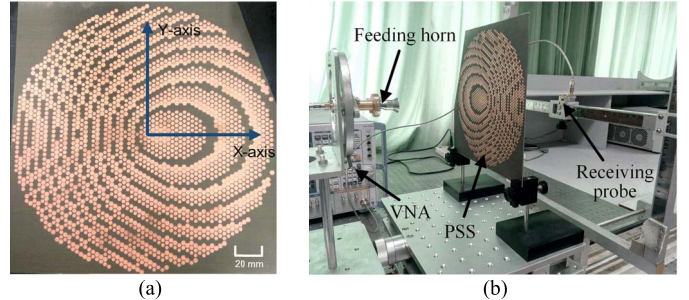


Fig. 13. (a) Prototype of the fabricated PSS. (b) Measurement setup of the antenna. (In order to show the whole measurement system clearly, the wave-absorbing material around the PSS is not shown in the figure).

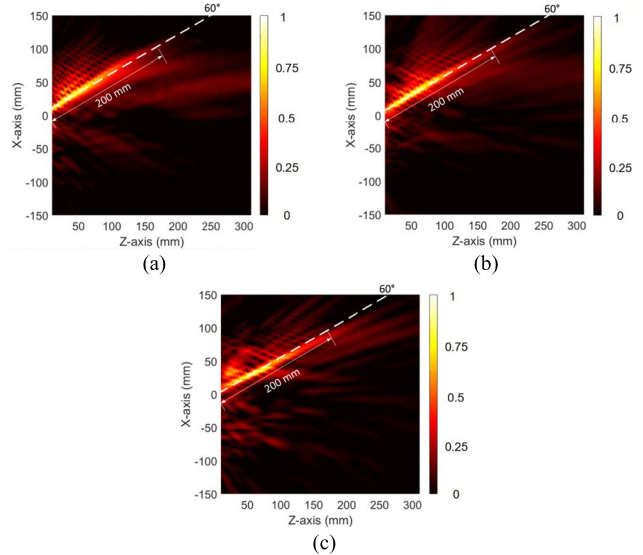


Fig. 14. Measured normalized magnitudes of the electric field in the $X Oz$ plane at different frequencies. (a) $f = 27$ GHz. (b) $f = 29$ GHz. (c) $f = 31$ GHz.

to the feeding horn, and the other port is connected to the near-field probe which has the same cross section as the standard waveguide WR28. The PSS is fed by a conical horn with the gain of 11.77 dBi. The outgoing wave from the feeding horn is the linearly polarized wave along the y -axis. The radiation pattern of the feeding horn is almost consistent in the band of 27–31 GHz. Under the comprehensive consideration of the element, the aperture, and the feeding horn [26]–[28], the focal

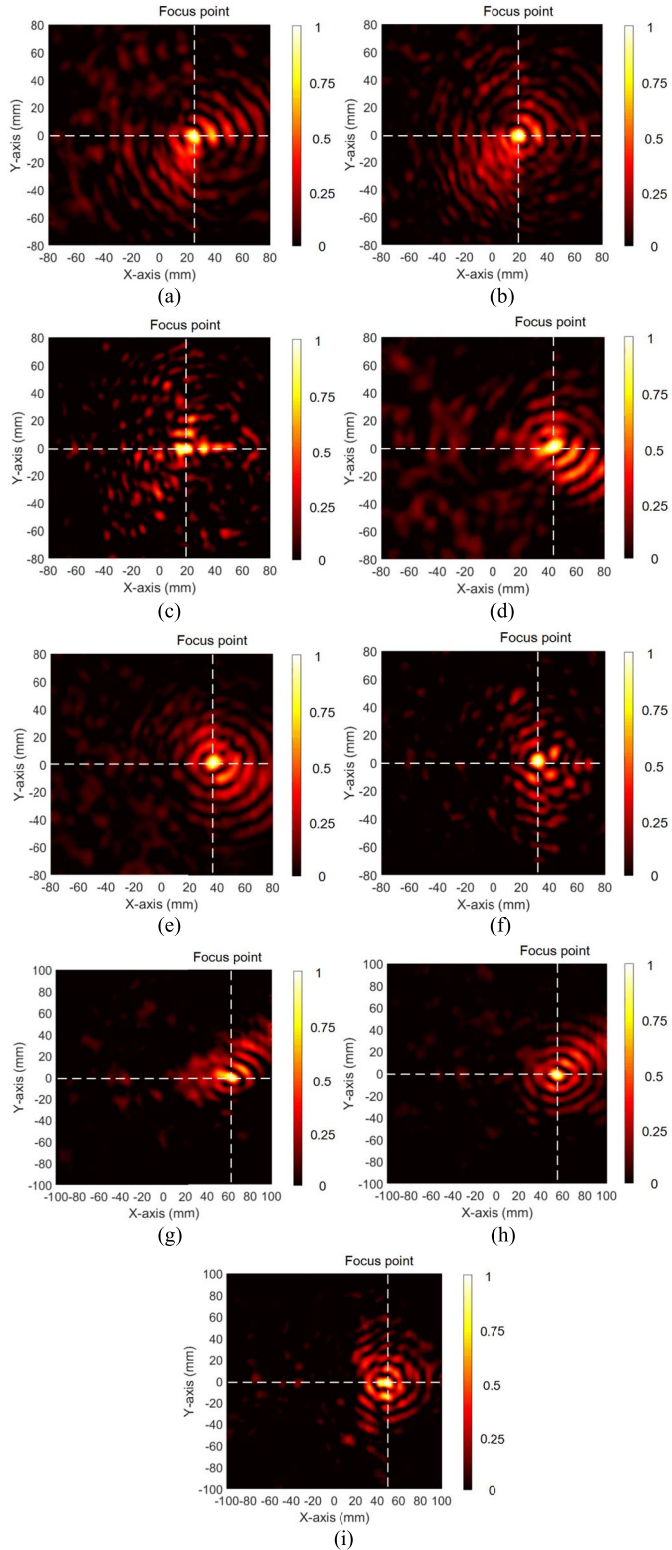


Fig. 15. Measured normalized magnitude of the electric field at different distances from the PSS z and different frequencies f . (a) $f = 27$ GHz, $z = 30$ mm. (b) $f = 29$ GHz, $z = 30$ mm. (c) $f = 31$ GHz, $z = 30$ mm. (d) $f = 27$ GHz, $z = 60$ mm. (e) $f = 29$ GHz, $z = 60$ mm. (f) $f = 31$ GHz, $z = 60$ mm. (g) $f = 27$ GHz, $z = 90$ mm. (h) $f = 29$ GHz, $z = 90$ mm. (i) $f = 31$ GHz, $z = 90$ mm.

length is properly selected as $d = 173$ mm, with a -10 dB edge illumination level at $\pm 30^\circ$ beam angle of the horn. The feeding horn and the center of the PSS are aligned by a laser.

The measured magnitudes of the y -polarized electric field in the XOZ -plane at different frequencies are shown in Fig. 14. The inclination angles of the beams are substantially maintained at the target value $\theta = 60^\circ$ over the entire band. The depth-of-field of the beams is also consistent with the design value $l = 200$ mm. The comparison of the profiles in Figs. 11 and 14 show that the simulated results are in good agreement with the measured results. Thanks to the phase shift compensation capability of the PSS, the maximum gap between the target and actual inclination angles decreases from 4° (as shown in Fig. 8) to 1.5° .

The distributions of the field on the transversal planes at different frequencies and at different distances from the PSS are shown in Fig. 15. The focused points are marked on the figures. The focused positions on the plane are coincident with the target positions. In addition, the ring-shaped field distribution outside the focused points shows a certain degree of the Bessel shape distribution. This is because the phase distribution of the pesudo-Bessel beam is employed in the design of the PSS.

The illumination efficiency and the radiation efficiency of the proposed PSS antenna are higher than 82% and 65% in the entire band, respectively. They are calculated by integrating the full-wave simulated Poynting vector at the incident side and the output side of the PSS, respectively. They represent the power illuminated on the PSS and transmitted from the other side of PSS, respectively. Both of them are normalized to the power radiated from the feeding horn.

V. CONCLUSION

A quasi-nondiffraction beam antenna with wideband and large depth-of-field is proposed in this paper. The propagating angle and the depth-of-field of the beam can be accurately controlled. The design methods of the zero-order pseudo-Bessel beam antenna and the multifocusing antenna are employed and combined in the design. One kind of PSS element with controllable phase shift in the band is employed. Its phase shift compensation capability can widen the bandwidth of the antenna as well as improve the stability of the antenna performance. The results of the calculation, the full-wave simulation, and the experiment agree well with each other. The proposed antenna can effectively generate the quasi-nondiffraction beam with controllable depth-of-field and propagating angle over a wideband.

REFERENCES

- [1] A. Mazzinghi *et al.*, "Large depth of field pseudo-Bessel beam generation with a RLSA antenna," *IEEE Trans. Antennas Propag.*, vol. 62, no. 8, pp. 3911–3919, Aug. 2014.
- [2] D. McGloin and K. Dholakia, "Bessel beams: Diffraction in a new light," *Contemp. Phys.*, vol. 46, no. 1, pp. 15–28, 2005.
- [3] J. Durnin, "Exact solutions for nondiffracting beams. I. The scalar theory," *J. Opt. Soc. Amer. A, Opt. Image Sci.*, vol. 4, no. 4, pp. 651–654, Apr. 1987.
- [4] Y. C. Zhong and Y. J. Cheng, "Large depth-of-field wideband pseudo-Bessel beam antenna," in *Proc. Eur. Microw. Conf. (EuMC)*, London, U.K., Oct. 2016, pp. 321–324.
- [5] Y. C. Zhong and Y. J. Cheng, "Ka-band wideband large depth-of-field beam generation through a phase shifting surface antenna," *IEEE Trans. Antennas Propag.*, vol. 64, no. 12, pp. 5038–5045, Dec. 2016.

- [6] S. Monk, J. Arlt, D. Robertson, J. Courtial, and M. Padgett, "The generation of Bessel beams at millimetre-wave frequencies by use of an axicon," *Opt. Commun.*, vol. 170, nos. 4–6, pp. 213–215, Nov. 1999.
- [7] N. Trappe, R. Mahon, W. Lanigan, J. A. Murphy, and S. Withington, "The quasi-optical analysis of Bessel beams in the far infrared," *Infr. Phys. Technol.*, vol. 46, no. 3, pp. 233–247, Mar. 2005.
- [8] Z. Li, K. B. Alici, H. Caglayan, and E. Ozbay, "Generation of an axially asymmetric Bessel-like beam from a metallic subwavelength aperture," *Phys. Rev. Lett.*, vol. 102, no. 14, p. 143901, 2009.
- [9] C. Pfeiffer and A. Grbic, "Controlling vector Bessel beams with metasurfaces," *Phys. Rev. Appl.*, vol. 2, no. 4, p. 044012, 2014.
- [10] M. Q. Qi, W. X. Tang, and T. J. Cui, "A broadband Bessel beam launcher using metamaterial lens," *Sci. Rep.*, vol. 5, Jun. 2015, Art. no. 11732.
- [11] M. Ettorre, S. M. Rudolph, and A. Grbic, "Generation of propagating Bessel beams using leaky-wave modes: Experimental validation," *IEEE Trans. Antennas Propag.*, vol. 60, no. 6, pp. 2645–2653, Jun. 2012.
- [12] P. Lemaître-Auger, S. Abielmona, and C. Caloz, "Generation of Bessel beams by two-dimensional antenna arrays using sub-sampled distributions," *IEEE Trans. Antennas Propag.*, vol. 61, no. 4, pp. 1838–1849, Apr. 2013.
- [13] M. F. Imani and A. Grbic, "Generating evanescent Bessel beams using near-field plates," *IEEE Trans. Antennas Propag.*, vol. 60, no. 7, pp. 3155–3164, Jul. 2012.
- [14] M. A. Salem, A. H. Kamel, and E. Niver, "Microwave Bessel beams generation using guided modes," *IEEE Trans. Antennas Propag.*, vol. 59, no. 6, pp. 2241–2247, Jun. 2011.
- [15] M. Albani, S. C. Pavone, M. Casella, and M. Ettorre, "Generation of non-diffractive Bessel beams by inward cylindrical traveling wave aperture distributions," *Opt. Exp.*, vol. 22, no. 15, pp. 18354–18364, Jul. 2014.
- [16] M. Ettorre, S. C. Pavone, M. Casella, and M. Albani, "Experimental validation of Bessel beam generation using an inward Hankel aperture distribution," *IEEE Trans. Antennas Propag.*, vol. 63, no. 6, pp. 2539–2544, Jun. 2015.
- [17] S. C. Pavone, M. Ettorre, and M. Albani, "Analysis and design of Bessel beam launchers: Longitudinal polarization," *IEEE Trans. Antennas Propag.*, vol. 64, no. 6, pp. 2311–2318, Jun. 2016.
- [18] J. Salo *et al.*, "Millimetre-wave Bessel beams using computer holograms," *Electron. Lett.*, vol. 37, no. 13, pp. 834–835, Jun. 2001.
- [19] N. Gagnon, A. Petosa, and D. A. McNamara, "Research and development on phase-shifting surfaces (PSSs)," *IEEE Antennas Propag. Mag.*, vol. 55, no. 2, pp. 29–48, Apr. 2013.
- [20] Y. J. Cheng, W. Hong, and K. Wu, "94 GHz substrate integrated monopulse antenna array," *IEEE Trans. Antennas Propag.*, vol. 60, no. 1, pp. 121–129, Jan. 2012.
- [21] Y. J. Cheng, H. Xu, D. Ma, J. Wu, L. Wang, and Y. Fan, "Millimeter-wave shaped-beam substrate integrated conformal array antenna," *IEEE Trans. Antennas Propag.*, vol. 61, no. 9, pp. 4558–4566, Sep. 2013.
- [22] J. Wu, Y. J. Cheng, and Y. Fan, "A wideband high-gain high-efficiency hybrid integrated plate array antenna for V-band inter-satellite links," *IEEE Trans. Antennas Propag.*, vol. 63, no. 4, pp. 1225–1233, Apr. 2015.
- [23] H. B. Wang and Y. J. Cheng, "Broadband printed-circuit-board characterization using multimode substrate-integrated-waveguide resonator," *IEEE Trans. Microw. Theory Techn.*, vol. 65, no. 6, pp. 2145–2152, Jun. 2017.
- [24] Y. J. Cheng and F. Xue, "Ka-band near-field-focused array antenna with variable focal point," *IEEE Trans. Antennas Propag.*, vol. 64, no. 5, pp. 1725–1732, May 2016.
- [25] H. B. Wang and Y. J. Cheng, "Frequency selective surface with miniaturized elements based on quarter-mode substrate integrated waveguide cavity with two poles," *IEEE Trans. Antennas Propag.*, vol. 64, no. 3, pp. 914–922, Mar. 2016.
- [26] M. R. Chaharmir, J. Shaker, and H. Legay, "Broadband design of a single layer large reflectarray using multi cross loop elements," *IEEE Trans. Antennas Propag.*, vol. 57, no. 10, pp. 3363–3366, Oct. 2009.
- [27] A. Yu, F. Yang, A. Z. Elsherbini, J. Huang, and Y. Rahmat-Samii, "Aperture efficiency analysis of reflectarray antennas," *Microw. Opt. Technol. Lett.*, vol. 52, no. 2, pp. 364–372, Feb. 2010.
- [28] A. Capozzoli, C. Curcio, A. Lisenò, and G. Toso, "Phase-only synthesis of flat aperiodic reflectarrays," *Prog. Electromagn. Res.*, vol. 133, pp. 53–89, Oct. 2013.



Yi Chen Zhong received the B.S. degree from the University of Electronic Science and Technology of China, Chengdu, China, in 2009, where he is currently pursuing the Ph.D. degree.

His current research interests include phase shift surface, nondiffracting beams, and near-field beam forming antennas.



Yu Jian Cheng (SM'14) was born in Sichuan, China, in 1983. He received the B.S. degree from the University of Electronic Science and Technology of China, Chengdu, China, in 2005, and the Ph.D. degree, without going through the conventional master's degree, from Southeast University, Nanjing, China, in 2010.

Since 2010, he has been with the School of Electric Engineering, University of Electronic Science and Technology of China, and is currently a Professor. From 2012 to 2013, he was a Research Staff with the Department of Electrical and Computer Engineering, National University of Singapore, Singapore. He has authored or coauthored more than 100 papers in journals and conferences, as well as a book *Substrate Integrated Antennas and Arrays* (CRC press, 2015). His current research interests include microwave and millimeter-wave antennas, and arrays and circuits.

Dr. Cheng was a recipient of the National Science Fund for Excellent Young Scholars in 2016, Chang Jiang Scholars Program (Young Scholars) in 2016, the National Program for Support of Top-Notch Young Professionals in 2014, New Century Excellent Talents in University in 2013, and National Excellent Doctorate Dissertation of China in 2012. He is a Senior Member of the Chinese Institute of Electronics, Beijing, China. He has served as an Associate Editor of the IEEE ANTENNAS AND PROPAGATION LETTERS and on review boards of various technical journals. He is currently the Secretary of the joint IEEE Chapters of APS/EMCS, Chengdu.